JGR Solid Earth

RESEARCH ARTICLE
10.1029/2024JB029223

The Influence of Mantle Structure on Dynamic Topography in Southern Africa

Kenneth C. Gourley[1] and **Christoper Harig**[1]

[1]Department of Geosciences, University of Arizona, Tucson, AZ, USA

Key Points:

- We generate Bayesian estimates of localized radial mantle viscosity and dynamic topography in southern Africa
- We model present-day vertical displacement of southern African using Global Navigation Satellite System station timeseries and Slepian localization techniques
- There is evidence for significant dynamic support (>1,000 m) and present-day vertical motion (1s: 0.8–2.0 mm/yr) due to mantle dynamics

Supporting Information:

Supporting Information may be found in the online version of this article.

Correspondence to:

K. C. Gourley,
kengourley@arizona.edu

Citation:

Gourley, K. C., & Harig, C. (2024). The Influence of mantle structure on dynamic topography in Southern Africa. *Journal of Geophysical Research: Solid Earth*, *129*, e2024JB029223. https://doi.org/10.1029/2024JB029223

Received 2 APR 2024
Accepted 8 OCT 2024

Author Contributions:

Conceptualization: Christoper Harig
Formal analysis: Kenneth C. Gourley
Funding acquisition: Christoper Harig
Methodology: Kenneth C. Gourley, Christoper Harig
Software: Kenneth C. Gourley, Christoper Harig
Supervision: Christoper Harig
Validation: Kenneth C. Gourley
Writing – original draft: Kenneth C. Gourley
Writing – review & editing: Kenneth C. Gourley, Christoper Harig

Abstract Due to relatively high terrain and negligible active tectonics, the southern Africa region boasts over 30 independent estimates of dynamic topography. These published estimates display a wide variance due to both the variety of methods used in computation and a lack of constraints on the regional mantle structure. Here we show that a focus on regional mantle structure is important to generate models of lithospheric and mantle dynamics. Global average mantle properties are not representative of a particular region, and it is necessary to generate viscosity profiles specific to a region of interest. We develop a Bayesian inversion using dynamic geoid kernels, existing seismic tomography models, and Slepian functions to invert for a localized radial viscosity profile that best explains the geoid in southern Africa. With an understanding of viscosity uncertainty, we constrain dynamic topography in southern Africa to lie between 1,000 and 2,000 m. Additionally, we model vertical displacements from 112 Global Navigation Satellite System stations across our region to examine the long-term, long wavelength pattern of present-day vertical motion, suggesting that a mean of 1.5 mm/yr (1σ: 0.8–2.0 mm/yr) of vertical motion may be related to ongoing dynamic topography. Our study demonstrates the utility of dynamic geoid kernels in local nonlinear inversions of non-unique geophysical data. Furthermore, we present evidence that the mantle beneath southern Africa is generating significant dynamic support for and vertical displacement of the lithosphere in this region.

Plain Language Summary The high topography of southern African is a result of the interaction between the lithosphere and the mantle beneath the region, a process referred to as dynamic topography. The viscosity of Earth's mantle is a primary driver of the buoyancy forces that generate this dynamic topography. There is significant disagreement regarding the amplitude and pattern of dynamic topography in this region, partially owing to the lack of constraints on inputs to geodynamic models, especially viscosity. We use the geoid to constrain mantle viscosity within our study region by combining existing statistical techniques in a novel manner. We generate models of mantle viscosity, dynamic topography, and present-day vertical displacement for our study region. Our preferred model results in 1,000–2,000 m of dynamic topography, suggesting that the whole of southern Africa is dynamically supported. We also find evidence for around 1.5 mm/yr (1σ: 0.8–2.0 mm/yr) of present-day vertical displacement within the southern part of the region, suggesting that dynamic topography is currently increasing. We argue that the viscosity within any given region of the mantle differs significantly from the whole-mantle average, and care must be taken to use a viscosity model that corresponds to the region of interest when creating geodynamic models.

1. Introduction

Convective forces and motions within Earth's mantle cause deformation of the lithosphere and the surface, the best known expression of this process being plate tectonics. These forces also cause vertical displacement of Earth's surface, commonly termed dynamic topography (Forte et al., 1993; Morgan, 1965a, 1965b; M. A. Richards & Hager, 1984). For the purposes of this study, we define dynamic topography similar to Molnar et al. (2015): the surface deformation due to normal tractions applied at the base of the lithosphere. This definition includes a narrower set of mantle processes than those employed by other studies (e.g., Holdt et al., 2022; Moucha & Forte, 2011), who allow buoyancy variations within the lithosphere to influence their prediction of dynamic topography. We consider such processes static and instead wish to focus on surface deflection due to mantle flow.

Southern Africa has been the subject of significant focus as a region with possible dynamic topography. Despite a lack of recent tectonic activity in this region, the Southern African Plateau exists at a relatively high mean elevation of almost 1,000 m (Al-Hajri et al., 2009) (Figure 1a). This region has been devoid of active orogeny, subduction, and widespread volcanic rocks for tens of millions of years (Pasyanos & Nyblade, 2007), yet

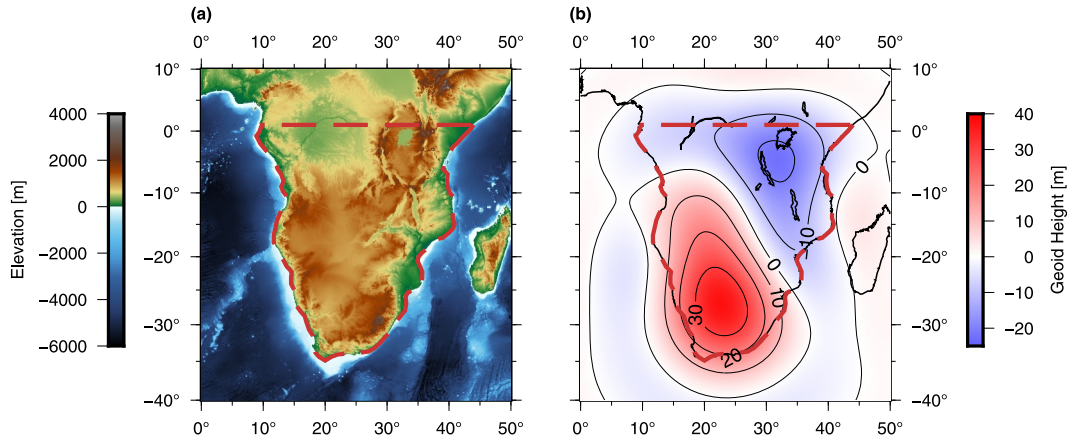

Figure 1. Maps of southern Africa showing (a) the topography and bathymetry of the region from ETOPO1 (Amante & Eakins, 2009); and (b) the non-hydrostatic geoid from EGM2008 (Pavlis et al., 2012) localized using Slepian techniques (see Section 2.2). The red dashed line in both maps denotes the outline of the study region. As shown in panel (a), the elevation of much of the plateau in our study region exceeds 1,000 m, with some parts extending up to 2,000 m in elevation. Meanwhile, the geoid in panel (b) remains relatively low within this same region.

significant removal of crustal material has occurred during the same time frame (de Wit, 2007). The combination of these factors has led many to draw the conclusion that the mantle must contribute to the plateau elevation.

The geoid over southern Africa (Figure 1b) gives a sense of the isostatic contribution to surface topography (Colli et al., 2016; Molnar et al., 2015; Ricard et al., 1984). The high values of the long-wavelength geoid, along with the existence of anomalously low seismic velocities beneath southern Africa (commonly attributed to upwelling) lend support to the idea that there is a moderate to large component of dynamic support in southern Africa (e.g., Flament et al., 2013; Lithgow-Bertelloni & Silver, 1998).

Over 25 studies performed over the past four decades have made predictions about the amplitude of dynamic topography in southern Africa. While most of these studies are through global geodynamic modeling, several focus on regional analyses in southern Africa. Despite the amount of attention the region has received, the results have yet to converge to a consensus range of possible dynamic topography values. These predictions span a wide range: 0 m (Forte et al., 2010), 200 m (Molnar et al., 2015), 300 m (Zhang et al., 2012), 300–600 m (Gurnis et al., 2000), 650–700 m (Lithgow-Bertelloni & Silver, 1998), and greater than 1,200 m (Flament et al., 2014). The significant disagreement between these estimates stems primarily from a lack of data in southern Africa. The region has both poor seismic station coverage and very few large seismic events, resulting in under-constrained tomographic images of the mid-to upper-mantle (Fishwick, 2010). Likewise, not enough receiver function and tectonic studies have been performed in southern Africa to provide conclusive data about density within the lithosphere (Sun et al., 2018). Without the proper data to constrain geodynamic models, the variance between studies remains high.

Here, we use the non-hydrostatic geoid as a constraint to invert for the viscosity of the mantle beneath southern Africa using Bayesian statistical analyses of instantaneous flow models. These inversions also result in estimates of dynamic topography that result from the mantle flow models. Additionally, we examine vertical Global Navigation Satellite System (GNSS) station motions, which we localize within southern Africa using Slepian functions. Our novel approach of combining geodynamic inversions with Slepian techniques allows us to gain unique insight into the mantle viscosity and surface dynamic topography of a specific region. This is in contrast to previous studies, which approximate regional properties based on global models. Our results are applicable to understanding the structure of the mantle beneath southern Africa, including that of the African large low-shear-velocity province (LLSVP), and how it influences mantle-induced surface deformation.

2. Methods

We use instantaneous geodynamic modeling and geoid constraints to invert for the mantle radial viscosity structure. We combine spatio-spectral localization (Simons et al., 2006) with Bayesian statistical techniques

(Sambridge et al., 2013) to compute both global and regional mantle viscosity profiles. Together, this analysis gives an informed estimate of the magnitude of dynamic topography in southern Africa. In addition, we generate an estimate of the current vertical displacement in southern Africa by inverting GNSS vertical station data.

2.1. Geoid and Surface Displacement Kernels

Following the method of Hager and Clayton (1989), we construct Green's functions that map mantle viscosity and density to surface observables. These kernels produce dynamic models of both the geoid and dynamic topography at the Earth's surface. The derivation of these Green's functions is briefly outlined below.

In order to calculate the deformation related to dynamics and the resulting geoid, we need to solve the equations of motion. These equations include self-gravitation and assume there is no hydrostatic reference stress or potential. Additionally, coupling between poloidal and toroidal components of flow is ignored, because lateral viscosity variations are assumed to be insignificant. We contend that this is case for our regional analyses (contained within the region outlined in Figure 1), where any heterogeneities in the mantle across our region are likely to be small (Moucha et al., 2007). We approximate the vertically heterogeneous mantle as a stack of homogeneous shell layers and solve the system by a propagator matrix technique to obtain the kernels. No-slip boundary conditions are applied between layers, and free-slip boundary conditions are applied at the Earth's surface and the core-mantle boundary (CMB).

Once these kernels are constructed, we linearly convolve the response function with a density model of the mantle to determine the total field. The potential field at the surface R is defined as

$$\mathcal{V}_{lm}(\mathbf{R}) = \frac{4\pi G R}{2l+1}\int_c^R \mathcal{G}^l(r)\delta\rho_{lm}(r)dr. \tag{1}$$

Here, $\mathcal{V}_{lm}(\mathbf{R})$ is the anomalous potential at the Earth's surface; r is the radial coordinate; l is the spherical harmonic degree; m is the spherical harmonic order; G is the gravitational constant; c is the CMB; $\mathcal{G}^l(r)$ is the geoid kernel, and $\delta\rho_{lm}(r)$ is the perturbed density model of the mantle as a function of depth. The displacement field at the surface is similarly defined as

$$H_{lm}(\mathbf{R}) = \frac{1}{\Delta\rho_R}\int_c^R \mathcal{A}^l(r)\delta\rho_{lm}(r)dr. \tag{2}$$

$H_{lm}(\mathbf{R})$ is the deformation at the Earth's surface; $\mathcal{A}^l(r)$ is the surface displacement kernel; and $\Delta\rho_R$ is the average density of the mantle. $\mathcal{V}_{lm}(\mathbf{R})$, $H_{lm}(\mathbf{R})$, and $\delta\rho_{lm}(r)$ are functions of spherical harmonic degree l and order m, while the geoid $\mathcal{G}^l(r)$ and surface displacement $\mathcal{A}^l(r)$ kernels are functions only of spherical harmonic degree.

We show geoid and surface displacement kernels for two simple models of the radial viscosity of the mantle (Figure 2). This method of mapping a mantle density structure to an instantaneous geoid and dynamic topography is computationally faster than time-dependent analytical models (e.g., Le Stunff & Ricard, 1997) and more precise than other instantaneous flow models (e.g., Lithgow-Bertelloni & Silver, 1998). The modern utility of this method is that it allows a wide range of model parameters to be explored within a timely manner, as discussed in Section 2.3.

2.2. Localization via Slepian Functions

Our regional analyses use Slepian functions to perform a spatio-spectral localization of the dynamic geoid kernels and surface data sets such as the geoid and dynamic topography. Slepian functions are well studied in the literature (e.g., Dahlen & Simons, 2008; Harig et al., 2015; Simons, 2010; Simons et al., 2006; Wieczorek & Simons, 2005), and here we present a brief overview of their construction.

Spherical harmonic functions, Y, are orthogonal over the whole sphere, Ω. When considered over a partial sphere region A, however, they are no longer orthogonal, and their integral products are no longer delta functions, instead forming a matrix with strong off-diagonal energy,

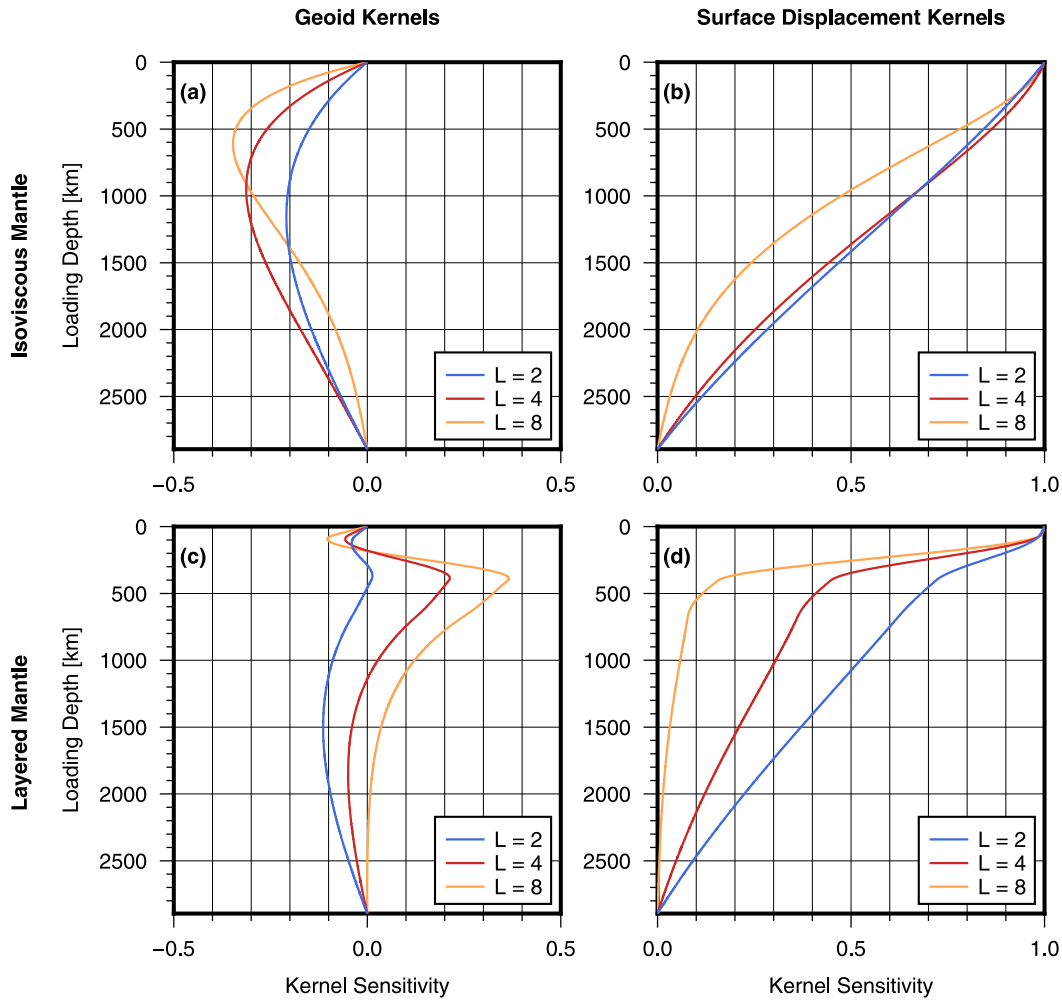

Figure 2. Plots of geoid kernels for (a) an isoviscous mantle and (c) a layered mantle; and the corresponding surface displacement kernels for the same (b) isoviscous mantle and (d) layered mantle. These are plotted as a function of loading depth (synonymous with mantle depth here) and spherical harmonic degree L. The layered case consists of a moderately strong lower mantle, weak mid mantle and asthenosphere, and strong lithosphere. Functions of progressively higher spherical harmonic orders sample shallower within the mantle. Also, complex models of mantle viscosity typically produce complicated weightings of mantle density structures. These plots are reproductions of parts of Figures 9.21 and 9.24 from Hager and Clayton (1989).

$$\int_A Y_{lm}\, Y_{l'm'}\, d\Omega = D_{lm,l'm'}. \tag{3}$$

We use the "localization kernel" matrix **D** to generate the new Slepian functions g by solving the eigenvalue decomposition such that

$$\sum_{l'=0}^{L} \sum_{m'=-l'}^{l'} D_{lm,l'm'}\, g_{l'm'} = \lambda g_{lm}. \tag{4}$$

The eigenfunctions of **D** then form a new basis which is both orthogonal over the region and over the whole sphere, where the eigenvalues $0 \leq \lambda \leq 1$ describe the portion of the function's energy concentrated within the region A. Here, l and m (and l', m') are the spherical harmonic degree and order, respectively.

We can form a regional basis by truncating the set of functions when eigenvalues become low. This sparse representation of data allows very good reconstruction properties within the region and limits influence from phenomena outside of our region of interest (Harig & Simons, 2012). In this study, we operate the dynamic geoid kernels with Slepian localization functions to create local geoid kernels, which are now localized in three-dimensional space. Thus, the regional viscosity inversions are based solely on the structure of the mantle beneath southern Africa.

Our study region is defined by the coastal outline of Africa for the southern, eastern, and western borders and latitude 1° N for the northern border (see Figure 1a). This region encompasses all areas of high elevation in southern Africa, besides that belonging to the northern portion of the east African rift system. The efficiency and sparsity of a Slepian representation leads to computational savings and reduces the non-uniqueness of the inverse problem. To accomplish this localization, we have sacrificed complete isolation of signals in the spectral domain. The basis functions are no longer delta functions in the spectral domain. While our basis has perfect localization in the spectral domain up to a bandlimit, each individual function has energy spread over each degree up to L instead of just a single degree.

2.3. Bayesian Algorithm

We invert for radial viscosity profiles and the corresponding models of dynamic topography by using trans-dimensional, hierarchical Bayesian inference (Sambridge et al., 2013), specifically a reversible-jump Markov-chain Monte Carlo (MCMC) algorithm (Green, 1995). The algorithm used in this study closely follows the methods outlined by Rudolph et al. (2015). It traverses a complex model space while searching for a global minimum, which we assume is the true model of the Earth's mantle. At each iteration of the MCMC algorithm, there is an equal probability of five outcomes: creation of a viscosity discontinuity at a random depth, deletion of a viscosity discontinuity at a random depth, moving a random viscosity discontinuity to a new random depth, changing the value of a random discontinuity, or changing the estimate of the variance of the data in the model. After one of these outcomes is chosen at random, the geoid kernels and corresponding geoid are re-computed based on the resulting viscosity profile.

Each run of the MCMC algorithm is initialized with a single relative viscosity discontinuity at a depth of 180 km, where the viscosity above this depth is one order of magnitude higher than that below it. This depth is chosen because it is a conservative estimate of where the lithosphere beneath southern Africa terminates, based on inspection of the seismic tomography models used in this study. It is also consistent with geodynamic (Globig et al., 2016) and seismologic studies (Fishwick, 2010; Pasyanos & Nyblade, 2007) of the African lithosphere.

During the first iteration, the geoid is calculated according to the method outlined in Section 2.1. If this is a regional model, the geoid is calculated using local dynamic kernels (Section 2.2). We calculate the misfit (quadratic norm) between the observed and calculated geoid (either globally or regionally). The viscosity structure is then perturbed through one of the five possible steps outlined above, and the geoid and misfit are computed again. This new misfit is then used to determine the likelihood function as

$$P(M|O) = \frac{1}{\sqrt{(2\pi)^n}} \exp\left(-\frac{\phi(O)}{2}\right). \tag{5}$$

Here, n is the number of spherical harmonic functions $\left(n = (L+1)^2\right)$; M is the proposed model; and O is the operator that yields the synthetic model of the geoid. The Mahalanobis distance, which is a statistical measure of the distance between the proposed model and the model distribution, is represented by $\phi(O)$. We compute $\phi(O) = \mathbf{W^T I W}$, where $\mathbf{W}$ is the model misfit (described above); $\mathbf{W^T}$ is the transpose of $\mathbf{W}$; and $\mathbf{I}$ is the identity matrix. The probability of acceptance for the new model is then

$$\min\left(1, \frac{P(M|O')}{P(M|O)} \frac{k+1}{k'+1}\right), \tag{6}$$

where k is the number of viscosity layers. The primed variables correspond to the proposed model, and the unprimed variables correspond to the previous model. This proposed model is either accepted or rejected, and the algorithm moves to the next iteration, where the above process is repeated for a new perturbation. Equations 5 and 6 are modified from Rudolph et al. (2015), whose implementation of Bayesian techniques and notation follows closely that of Kolb and Lekić (2014).

We run each inversion for 1 million iterations, with the expectation that the model requires such a high number of iterations to converge at a solution. We computed several inversions for 2 million iterations as a means to verify that we use enough iterations to allow the models to find the global minimum. The ensemble averages of these tests at 2 million iterations are not significantly different from those at 1 million iterations. This gives us confidence that our resulting models of mantle viscosity are both well-constrained by the observed geoid and close to the global minimum of our model space. We compute the resulting ensemble average for a given inversion from the final two hundred thousand iterations. Since the ensemble average is a statistical entity and not physically meaningful, we use the viscosity profile from the final iteration as our solution to each inversion. We then pass the final viscosity profile back into the corresponding forward model to create updated kernels, which calculate the resulting predicted dynamic topography. This scheme ensures that the computation of dynamic topography uses the same model parameters as each of our corresponding inversions for the geoid. Namely, we use the same framework as Hager and Clayton (1989) with a depth above which density is ignored of 180 km: we apply free-slip boundary conditions at both the surface and CMB; apply no-slip boundary conditions between layers; and include self-gravitation.

We run both global and regional viscosity inversions over a range of 16 different mantle density models. For each analysis, we create a given density model by multiplying an existing shear wave seismic tomography model with a seismic scaling profile, $R_{\rho/s} = d[\ln \rho]/d[lnV_s]$. $R_{\rho/s}$ converts shear wave velocity to density as a function of depth within the mantle. The sign of $R_{\rho/s}$ implies the source of the V_s perturbation: a positive scaling profile corresponds to a thermal source, while a negative scaling profile corresponds to a compositional source. We use four different whole-mantle global tomography models: S40RTS (Ritsema et al., 2011), SEMUCB-WM1 (French & Romanowicz, 2014), SAW642ANb (Panning et al., 2010), and S362WMANI+M (Moulik & Ekström, 2014). We combine these tomography models with four different seismic scaling profiles: the "thermal velocity-density" scaling relationship produced by Simmons et al. (2007) and three depth-constant scaling profiles with values 0.2, 0.3, and 0.4. Additionally, we run a single regional model using S40RTS and the scaling profile from Steinberger (2016). The implication of these different scaling profiles is explored in the Discussion. We choose four distinct seismic tomography models to examine the effect of the variance between these models on the resulting mantle viscosity profiles and dynamic topography. All four tomography models were created within the past 15 years, ensuring reasonable data coverage beneath southern Africa. These are also all global shear-wave velocity models, allowing direct comparison between global and regional inversions.

Several regional seismic tomography models exist for southern Africa (e.g., Begg et al., 2009; Emry et al., 2019), but we chose not to use them for our study. These models have improved resolutions of the crust and upper mantle, but contain little to no data below depths of 400 km. Although our regional inversions are not heavily influenced by the lower mantle, placing no constraints on depths below 400 km would skew our models toward unrealistic results. We instead use four global tomography models with average to above average coverage for the whole mantle beneath southern Africa.

Our observed geoid, the primary constraint on our viscosity inversions, is that of EGM2008 (Pavlis et al., 2012) truncated between spherical harmonic degree and order 2 and 20, since higher-degree spherical harmonics primarily sample the upper mantle and crust. For our regional inversions, both the observed and computed geoid are localized to our region for comparison. We set 3,200 kg/m^3 as the average density of the mantle. The mantle tomography models are discretized at a depth interval of 10 km to resolve all structures large enough to be detected at degree 20. We zero out the density contributions from layers shallower than 180 km when computing the model geoid. As mentioned above, 180 km is a conservative estimate of the depth of the lithosphere beneath southern Africa. We do not want the lithosphere to contribute to our calculations of dynamic topography. Each inversion is allowed to insert at most 9 viscosity discontinuities in addition to the initial fixed discontinuity at the base of the lithosphere. We impose this condition to limit the complexity of our final models.

2.4. GNSS Vertical Displacement

In addition to our modeling work, we use long-term vertical GNSS timeseries to analyze the vertical displacement in southern Africa. We collect these timeseries from 112 stations hosted by the University of Nevada Reno Geodetic Laboratory (Blewitt et al., 2018). These stations lie within the same region as defined for the Bayesian inversions. Only stations with data spanning a period of at least 3 years were chosen for our analysis. We use the geodetic program Hector (Bos et al., 2013) to compute the linear vertical displacement rate for each station.

We project these rates into a Slepian basis and localize them within our region to form a spatial map, allowing for straightforward comparison with the estimates of dynamic topography. Our Slepian basis covers the same bandwidth as the Bayesian inversions ($2 \leq L \leq 20$), ensuring that all energy in this new basis is representative of only regional motions. By removing higher order spherical harmonics, we also remove station-dependent effects in areas with good station coverage. See Knowles et al. (2020) for a more detailed review of the utility that Slepian localization techniques provide to the estimation of regional motion with GNSS timeseries.

The resulting Slepian basis of GNSS-derived vertical displacements contains signal from processes such as changes in terrestrial water storage and glacial isostatic adjustment (GIA). In order to isolate the signal of displacement due to mantle dynamic processes, which will allow us to make inferences about the present-day generation of dynamic topography, we correct the GNSS linear displacement trends with data from the Gravity Recovery and Climate Experiment (GRACE) and follow on mission. We use the Center for Space Research (CSR) release level 5 (GRACE) data (Save et al., 2016), adding back the atmosphere and ocean model which is removed by default. We convert the time variable gravity signals from GRACE into vertical displacement by multiplying the gravitational potential with Farrell's load Love numbers (Farrell, 1972; Wahr et al., 1998) and then summing over each Slepian coefficient, in the same manner as Knowles et al. (2020). This product should also contain temporal geopotential trends due to tectonic/dynamic motions, but the magnitude would be dwarfed by any signals from the surface water cycle. By computing the linear trend of vertical displacement based on this GRACE data set and projecting these trends into a Slepian basis, we effectively model the effects of GIA, changes in present-day water storage, and trends in atmospheric pressure within our study region. Signal from these three processes are contained in the GNSS data set, and subtracting this GRACE-based model from our GNSS-based model results in a model that contains signal only from long wavelength, regional vertical motions. We perform this same correction for the GNSS station vertical uncertainties.

3. Results

3.1. Mantle Viscosity

For each of our 32 Bayesian inversions, we plot the ensemble viscosity interface probability distributions as a function of depth within the mantle. Here we discuss results of the inversions that use S40RTS as the seismic tomography model (Figure 3), while the results for the other tomography models are available in the Supporting Information S1. These distributions illustrate the depth and viscosity of layers preferentially inserted by the inversion for the final two hundred thousand iterations. The black line represents the ensemble average of the final iterations for each inversion and should not be interpreted as the mantle final viscosity profile.

The interface distributions for the global inversions (Figure 3, top row) with constant scaling profiles (b)–(d) are consistent between all of the seismic tomography models. These inversions all produce a strong lithosphere, a weak asthenosphere and upper-mantle, a strong mid-mantle, and a weak lower-mantle. The mean ensembles for each of these inversions are all smoothly varying, owing to the wide spread of potential inversion solutions. This is in contrast to the level of complexity seen in each of the global inversions that use the Simmons et al. (2007) scaling profile (e.g., Figure 3a). While the exact depth and values of viscosity interfaces vary for each inversion, the overall pattern is consistent: strong lithosphere, weak asthenosphere, strong mantle transition zone, weak layer at or below 1,000 km, strong layer in the upper portion of the lower-mantle, and a very weak lowermost mantle. This same viscosity distribution as a function of depth is not observed in any of the $R_{\rho/S} = constant$ global inversions, suggesting that the model constraints used to create the Simmons et al. (2007) scaling profile heavily control the output of our corresponding viscosity inversions.

The interface distributions for the regional inversions (Figure 3, bottom row) differ substantially from those of the global inversions in their overall pattern, model spread, and complexity. These model solutions tend to favor a

10.1029/2024JB029223

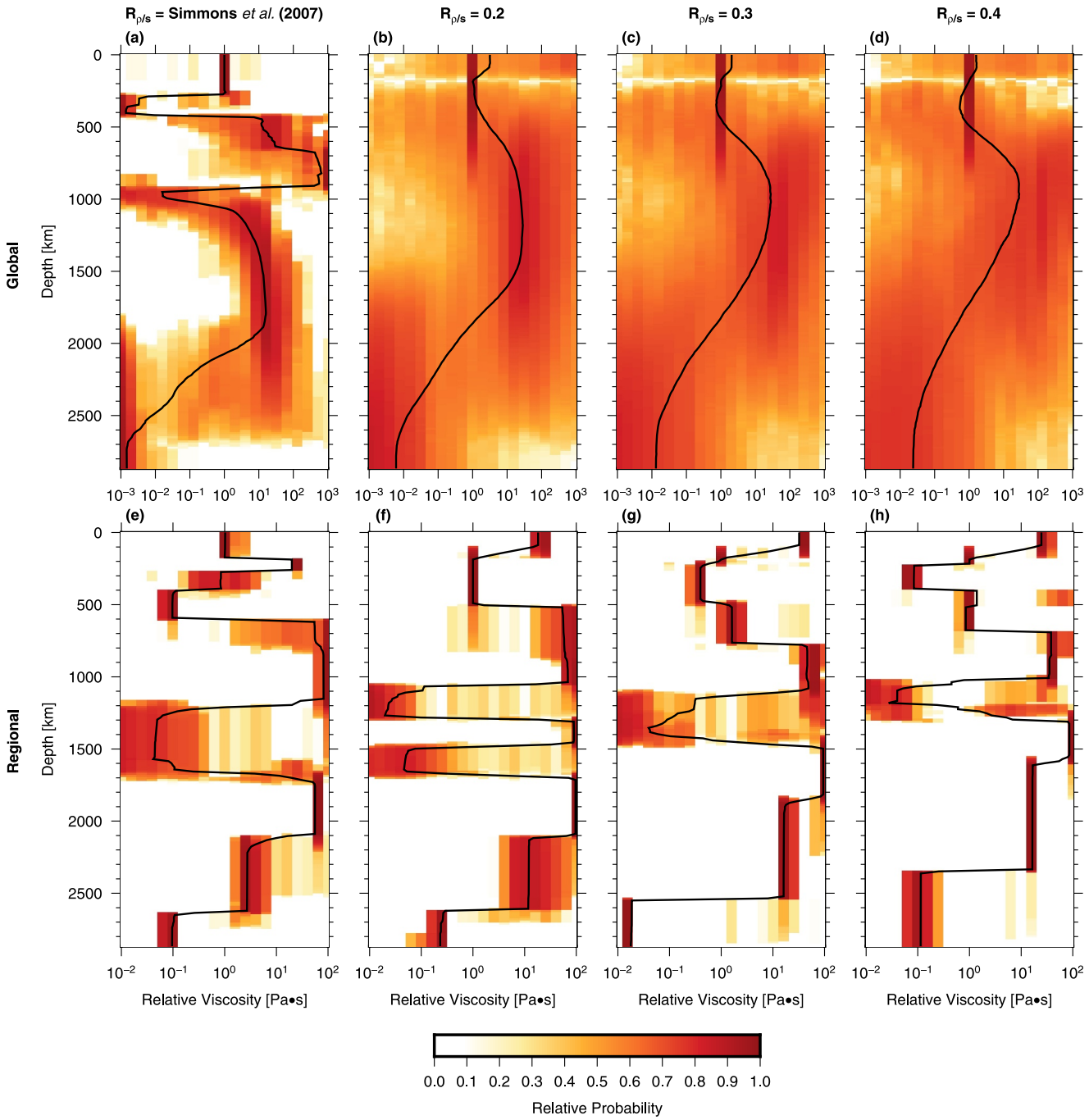

Figure 3. Viscosity inversion ensemble solutions for tomography model S40RTS. The top row (a–d) contains the results of the global inversions, while the bottom row (e–h) contains the results of the regional inversions. Each column contains the results for a different scaling profile; from left to right: (a, e) Simmons et al. (2007); (b, f) 0.2; (c, g) 0.3; and (d, h) 0.4. The black line in each plot is the ensemble average viscosity profile for the final two hundred thousand iterations of the inversion. The color gradient represents the normalized probability for the insertion of an interface at a specific depth and viscosity value.

strong lithosphere, weak asthenosphere and mantle transition zone, strong mid- and lower mantle, and weak base of the mantle. The spread of ensemble solutions as a function of viscosity is quite tight (typically less than 0.2 $Pa \cdot s$), except in the top of the lower mantle (specifically, between depths of 1,000 and 1,700 km). At these depths, the regional inversions slightly favor a low viscosity channel, but due to the ensemble spread, a higher viscosity is also somewhat likely for this depth range and would be more compatible with the viscosities of the layers immediately above and below. There is also greater consistency between ensemble solutions for the

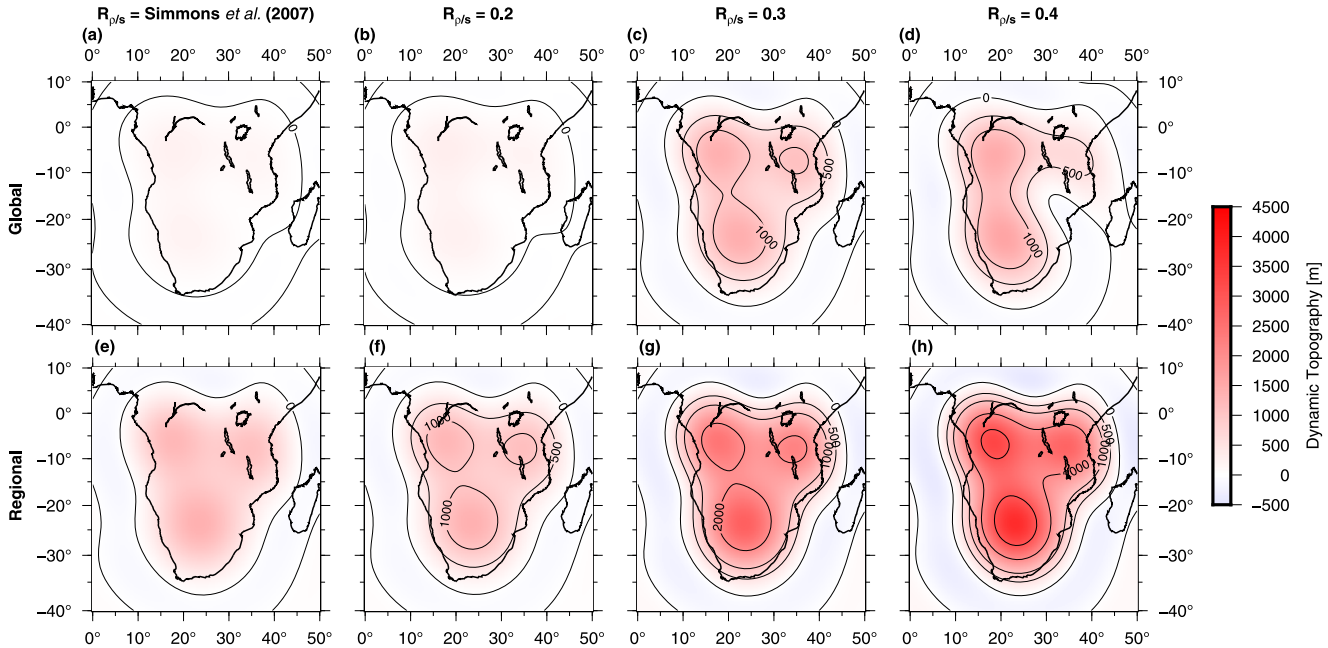

Figure 4. Predicted dynamic topography for tomography model S40RTS. The top row (a–d) contains the results of the global inversions, while the bottom row (e–h) contains the results of the regional inversions. Each column contains the results for a different scaling profile; from left to right: (a, e) Simmons et al. (2007); (b, f) 0.2; (c, g) 0.3; and (d, h) 0.4. The dynamic topography is shaded and contoured (at 500, 1,000, 2,000, 3,000, and 4,000 m) based on amplitude. All plots have been localized in the southern Africa region defined for this study for ease of comparison.

regional inversions as opposed to the global inversions when comparing the Simmons et al. (2007) scaling profile with the $R_{\rho/S}$ = constant scaling profiles.

3.2. Dynamic Topography

The synthetic surface dynamic topography computed from the final iteration of each Bayesian inversion is displayed in the same arrangement as the viscosity ensemble results, with global results in the top row and regional results in the bottom row. We show results utilizing S40RTS here (Figure 4) with the dynamic topography solutions for additional tomographic model results in the Supporting Information S1. In the global cases, dynamic topography is calculated globally and then localized using Slepian functions to our region for ease of comparison with the regional inversions.

The range of amplitudes for each plot of dynamic topography exhibits significant variance. In general, the amplitude of dynamic topography increases from left (Simmons et al. (2007) scaling) to right ($R_{\rho/S} = 0.4$) in each figure due to the general increase in density (and thus buoyancy force). For example, the regional $R_{\rho/S}$ = Simmons et al. (2007) solution has a maximum amplitude below 500 m, while the regional $R_{\rho/S} = 0.4$ solution has a maximum amplitude that exceeds 3,000 m. When comparing the solutions from different seismic tomography models with the same scaling profile, the amplitudes are consistent. Similarly, the pattern of dynamic topography is consistent among the results from each seismic tomography model. Overall, the input seismic tomography model is the primary control on the pattern of surface dynamic topography, while the scaling profile is the primary control on the amplitudes.

The amplitudes of dynamic topography for the regional inversions are greater than the amplitudes for each corresponding global inversion. In most cases, the amplitudes are modest, ranging from 200 to 1,000 m. Several inversions produce amplitudes greater than 2,000 m, most notably the regional models using the $R_{\rho/S} = 0.3$ and 0.4 scaling profiles. Another consistent feature between the models of dynamic topography is the presence of three lobes (Figures 4a–4h): one in the south, one in the northwest, and one in the northeast. In each model solution, all three lobes have amplitudes 200–300 m higher than the amplitude of the rest of our region. Outside of the three lobes, predicted dynamic topography is fairly uniform. These three lobes are also present in the models

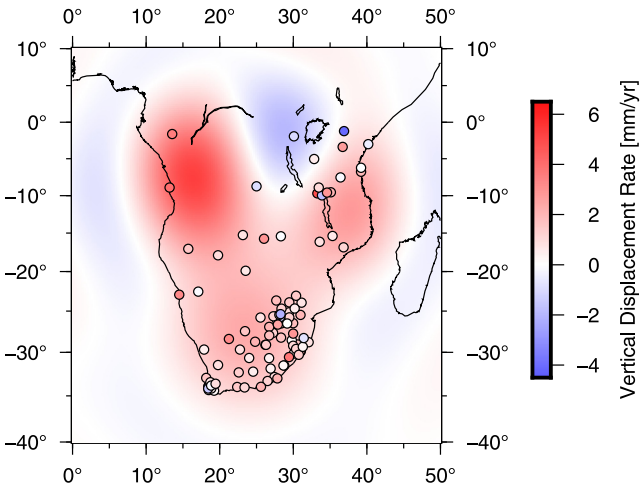

Figure 5. Long-term vertical rates from GNSS within our study region. Individual station motions are plotted as filled circles. The localized regional motion is plotted as a color gradient. Areas in the northern part of our region have the highest velocity amplitudes as well as the highest uncertainties due to the poor station coverage in these areas. The corresponding map of uncertainty can be found in the (Figure S8 in Supporting Information S1).

based on the three other seismic tomography models (Figures S5–S7 in Supporting Information S1), although the southern lobe dominates the other two lobes in these solutions.

3.3. Vertical GNSS Motions

The localized, corrected GNSS vertical motions are displayed in Figure 5, and the corresponding uncertainties are displayed in Figure S8 in Supporting Information S1. The filled circles represent the individual station motions, while the color gradient represents the motions localized into our regional Slepian basis. Regional uncertainty generally scales inversely with station density. Regional motions are therefore well determined south of a latitude of roughly 20°S, based on the overall uncertainty within this sub-region. The amplitude of the GRACE correction is low relative to that of the uncorrected signal—up to 0.7 mm/yr in a limited portion of our study area—with a regional average of 0.17 mm/yr.

Across southern Africa we see mostly broad, low magnitude, and positive vertical motions (Figure 5). The magnitude of these motions ranges from −1 to 6 mm/yr across the entire region. In the southernmost part of our region (south of −15°S), which has the highest station density, the mean vertical motion is 1.5 mm/yr (1σ: 0.8–2.0 mm/yr). There is a northwest lobe with vertical motion exceeding 6 mm/yr and a small north central sub-region which exhibits low amplitude negative vertical motions. This particular pattern is driven by four proximal stations with negative velocities. The pattern of vertical motions is somewhat similar to the pattern of dynamic topography resulting from several of the models in Section 3.2. There are three primary lobes of positive motion in the south, northwest, and northeast parts of our region, although the amplitude of the southern lobe is more subdued than those of the northern lobes. Our confidence in the two positive northern lobes, especially the northwest lobe, is low due to the poor station density and high uncertainty of the signal from these few stations in both sub-regions.

4. Discussion

4.1. Constraints on Mantle Viscosity Structure

In comparing the results of our regional viscosity inversions, it is clear that the choice of seismic tomography model has a strong effect. Our regional inversions that use S40RTS (Ritsema et al., 2011) as the input seismic tomography model (Figures 3e–3h) produce fewer discontinuities that alternate between low and high viscosity than the regional inversions that use the other three seismic tomography models in this study (Figures S1–S3e–h in Supporting Information S1). This alternating viscosity pattern is especially favored by the regional inversions which use S362WMANI+M (Figures S3e–S3h in Supporting Information S1), likely owing to the whole-mantle anisotropic nature of that model (Moulik & Ekström, 2014). Such alternations in viscosity confined to thin (approx. 200 km thick) layers are not compatible with our knowledge of heat diffusion in Earth's mantle (Bercovici et al., 2000).

Following the above reasoning, we favor the regional inversions that use S40RTS, as the resulting viscosity profiles contain smoother, more physically feasible depth variation. The results of these four regional inversions all contain one or more low viscosity channels between 1,000 and 1,700 km depth. Only the inversions that use the $R_{\rho/S}$ = Simmons et al. (2007) (Figure 3e) and the $R_{\rho/S} = 0.3$ (Figure 3g) scaling profiles produce mid-mantle low viscosity channels that are more than several hundred kilometers thick. Additionally, the $R_{\rho/S}$ = Simmons et al. (2007) inversion does not produce a strong lithosphere, unlike the other three scaling profiles. For these reasons, we select the $R_{\rho/S} = 0.3$ with S40RTS regional inversion as our preferred model of mantle viscosity beneath southern Africa.

Our preferred model of radial viscosity is similar to the results of both Mitrovica and Forte (2004) and Rudolph et al. (2020), who both perform inversions for global radial mantle viscosity. Both of these studies see the same viscosity discontinuity just below the mantle transition zone and a low viscosity channel in the mid-mantle.

Unique to our model, though, is the presence of a low viscosity channel in the middle of the mantle, between depths of 1,100 and 1,500 km. It is important to note, however, that although the ensemble average favors a low viscosity at these depths, a significant proportion of the ensemble models favor much higher viscosities which then do not produce this low viscosity channel. Overall, our inversion produces a wide range of potential viscosities for this zone of depths in the middle of the mantle.

We compute global inversions to compare with the regional models to judge the utility of regional inversions. The results of our global inversions all have wide uncertainty across the entire depth-range of the mantle (Figure 3). This is exemplified by both the viscosity spreads and smoothness of the ensemble averages for each of these inversion results, especially in the $R_{\rho/S} = constant$ cases. As expected, there are not enough constraints from the global geoid alone to allow for the estimation of radial mantle viscosity. Additionally, given the general complexity of mantle deformation and rheology (e.g., Jackson & Faul, 2010; Yang & Gurnis, 2016), this type of radial profile is likely not applicable to our study region, as a global inversion incorporates mantle dynamic processes not present in southern Africa (e.g., subduction zones and mid-ocean ridges). It is likely that a global average viscosity profile is not representative of any one particular region (see also Lau et al. (2018)), so using such a profile to produce geodynamic models in our study region is, therefore, problematic, and caution is warranted for regional studies.

The regional Bayesian inversions allow our analyses to examine effective lateral variations in viscosity within the Earth's mantle by solving for radial viscosity profiles in different regions. The localization of the geoid kernels ensures the regional inversions are influenced only by the structure of the mantle beneath southern Africa. The localization process itself is flexible and can be easily applied in different regions. One caveat is that the region must not be too small for the given bandwidth L considered. In this case, the Slepian basis would contain too few functions with acceptable eigenvalues (Simons et al., 2006). The same issue essentially applies in the depth dimension for different reasons. As depth within the mantle increases, the contributions to the surface gravity field can only be determined at long-wavelengths, which are inherently less well localized (Hager & Clayton, 1989; Hager et al., 1985). If the region of interest is small, the resulting geoid field will not contain much energy from lower mantle processes. The Bayesian inversion for viscosity will then be imprecise at greater depths, as it will try to constrain physical parameters for which it has little to no data.

Our inversions incorporate several assumptions about the structure of the mantle and lithosphere. In the global inversions, the relative viscosity profile is allowed to vary by six orders of magnitude, and we expect that this will encompass all possible values of viscosity within the mantle (e.g., Stadler et al., 2010). For regional inversions, the relative viscosity profile is allowed to vary by only four orders of magnitude. This narrower range lowers the number of iterations necessary for our inversion to converge upon a final solution. We do not believe that the narrower range will bias the regional inversions toward inserting more viscosity discontinuities to account for the smaller magnitude of these interfaces, depending on the overall smoothness of the input density model. In fact, it seems likely that viscosity will not vary greatly, since there is likely little lateral variation in viscosity within a given region of interest (Moucha et al., 2007).

We explore several different shear-wave velocity to mantle density scaling profiles, including those that are constant ($R_{\rho/S} = 0.2$, 0.3, and 0.4) and heterogeneous ($R_{\rho/S}$ = Simmons et al. (2007) and $R_{\rho/S}$ = Steinberger (2016)), to examine their impact on the inversion results. The constant scaling profiles assume a purely thermal contribution to seismic velocity heterogeneity throughout the mantle, which is not supported by recent seismic and geodynamic studies (Lau et al., 2017; Moulik & Ekström, 2014; F. D. Richards et al., 2023; Ritsema & Lekić, 2020). We include the Simmons et al. (2007) scaling profile, as it was specifically created to represent the thermochemical heterogeneities present in our study region. The single regional model that we compute using the Steinberger (2016) scaling profile (Figure S4a in Supporting Information S1) demonstrates the effect of using a constant scaling profile (i.e., $R_{\rho/S} = 0.3$) with regard for the thermochemical structure of the uppermost and base of the mantle. Even with the moderate heterogeneity in this additional scaling profile, the resulting viscosity profile is remarkably similar to our preferred scaling profile (compare Figures S4a with S4b in Supporting Information S1). There is inherent uncertainty in these conversions, and we invite the reader to look at Lee et al. (2011) for a more detailed analysis. Without better constraints from mineral physics and seismology on compositional heterogeneity (Simmons et al., 2009), especially within the African LLSVP, our choice of scaling profiles attempts to broadly cover the model space.

Our use of positive (thermal anomalies only) scaling profiles is justified based on the depth range of the largest chemical anomalies in the mantle. These chemical anomalies are at the base of the mantle, which is also where the sensitivity of our geoid kernels is lowest (see Figure 2c), resulting in there being little impact on the computed geoid from these anomalies. Despite the differences between each of the individual scaling profiles, the regional inversion results for any given seismic tomography model show strong similarities. The only major exception is in the middle of the mantle, which has the poorest coverage in our region for all of the seismic tomography models we use.

Our preferred viscosity model suggests that there is internal layering within the African LLSVP, with a strong top 600 km and very weak bottom 400 km, assuming a 1,000 km total thickness (Lekić et al., 2012). There are other geodynamic studies who argue for internal density layering within LLSVPs, consisting of a dense base overlain by a much lighter layer (Liu & Zhong, 2015; F. D. Richards et al., 2023). A vertical rheological heterogeneity appears in our results, and taken together with these other studies, this suggests some sort of layering is present within LLSVPs, whether it be of thermal or chemical origin.

4.2. Dynamic Topography

Our preferred model (Figure 4g) produces dynamic topography around 1,000 m across most of the region with three lobes (south, northeast, and northwest) that extend just beyond 2,000 m. These three sub-regions are also roughly where the highest topography currently exists (Figure 1a). Our model predicts higher amplitudes of dynamic topography than back-of-the-envelope studies, which predict dynamic topography to be on the order of 200 m (e.g., Molnar et al., 2015). Our results are somewhat comparable to, although slightly higher than, models that use observations of residual topography to constrain dynamic topography, most of which predict around 800–1,000 m of dynamic topography (Davies et al., 2019; Hoggard et al., 2016). Our preferred model is also modest compared to several instantaneous and time-integrated models, which claim dynamic topography in southern Africa exceeds 2,000 m (e.g., Forte et al., 1993; Steinberger et al., 2017). Nonetheless, the $R_{\rho/S}$ = Simmons et al. (2007) scaling profile predicts at least 400 m of dynamic topography, which is more than double the maximum estimate from Molnar et al. (2015).

Based on the range of dynamic topography in our preferred model and the amount of present-day topography, we argue that the southern African lithosphere is almost entirely dynamically supported by the mantle. Given that our estimate of dynamic topography exceeds the present-day topography in some sub-regions, particularly the north central part of our region, erosional forces might be competing with the upward mantle motion (Moucha & Forte, 2011). Although, Bierman et al. (2014) found slow erosion rates (approx. 5 m/Myr) across the southern part of our region since the Pliocene, so these erosional forces likely provide little resistance to any ongoing formation of dynamic topography.

It is important to note some of the same caveats about our choice of shear wave velocity to density scaling profiles as in Section 4.1. When comparing our results, the estimated dynamic topography is a strong function of scaling profile, with even a small increase from $R_{\rho/S} = 0.2$ to 0.3 doubling the overall amplitude (Figures 4f, and 4g). For more detailed overviews of how the computation of dynamic topography is affected by the choice of mantle structure, we invite the reader to look at Davies et al. (2019) and Flament (2019). Based on our results, even with a well-constrained viscosity profile for a specific region, there needs to be some degree of knowledge about the thermochemical properties of the mantle to accurately predict dynamic topography. We expect that both the viscosity and the seismic wave speed to density scaling profile change as a function of location within the mantle (e.g., Lau et al., 2018; F. D. Richards et al., 2023). Future work should investigate placing tighter constraints on the regional scaling profile based on seismic and geodynamic inferences, as suggested by Rudolph et al. (2020).

All of our inversions are constrained by the geoid using spherical harmonic degrees 2–20. Previous geodynamic studies of dynamic topography use a much narrower range of geoid data, with most extending out to degree and order 8 or 10 (e.g., Flament et al., 2013; Hager et al., 1985; Molnar et al., 2015). We contend that a wider bandwidth is necessary to better characterize the magnitude and spatial pattern of dynamic topography. As suggested by Davies et al. (2019), the global spectra of residual topography contains significant power out to degree and order 30, yet most instantaneous-flow simulations have power out to only degree and order 5. We do not extend our analyses beyond degree and order 20, because crustal effects dominate at higher orders (Hoggard

et al., 2016). Additionally, the global tomography models used in this study contain minimal power above degree and order 20, preventing us from constraining models at these higher orders.

This technique of computing regional viscosity profiles will prove useful in other regions where there is contention over the amplitude of dynamic topography. The region surrounding the New Hebrides Trench near Vanuatu and New Caledonia appears to be experiencing uplift related to slab detachment (Chatelain et al., 1992). Meanwhile, the Brazilian Highlands are at a relatively high elevation - on the order of 2,000 m—yet are not near any major surface tectonic features (Flament et al., 2014). Dynamic topography has been attributed to both regions, yet estimates of the amplitudes are not in good agreement. The methods presented in this paper could elucidate the magnitude of the mantle dynamic processes that control these features.

4.3. Vertical Displacement

Three lobes of positive vertical motion are displayed in the GNSS vertical motions (Figure 5), all of which correlate with the three lobes of dynamic topography in the south, northwest, and northeast parts of our region. The southern lobe is well-constrained by a dense station network, indicating that the roughly 1 mm/yr of vertical motion there is a real feature. The other two lobes do not have the same station coverage, which is reflected in the high uncertainty in these sub-regions. The northwest lobe is in the same sub-region as that determined by Walford and White (2005) to have experienced uplift over the last 30 Myr, as evidenced by erosional unconformities in seismic reflection data. These three lobes also correspond to areas of slight signal enhancement (less than 20% across the majority of each lobe) due to the Slepian localization techniques used in this study (Figure S9 in Supporting Information S1). It is likely that at least a portion of the vertical motion recorded by GNSS stations in these regions is due to regional uplift; however, it is not as high as indicated by the results of our analysis. These stations are recording non-geodynamic signals, and the low station density reduces our confidence in the vertical motions computed in these sub-regions. More station coverage and longer baselines are necessary to better constrain the amplitude of these features.

The vertical GNSS velocities computed in this study are similar to those estimated by both Hammond et al. (2021) and Saria et al. (2013). This gives us confidence that most of the stations used in this study have long enough baselines to reflect ongoing dynamic topography changes, as the rates are consistent through several decades of recording. In particular, Hammond et al. (2021) note that the long wavelength, coherent vertical displacement in southern Africa likely reflects a mantle geodynamic source. Based on these results, it is reasonable to conclude that up to between 0.8 and 2.0 mm/yr of uplift is occurring in southern Africa. Care should be taken extending such a rate backwards in time, as it does not account for denudation or variations in the uplift rate through time, both of which are non-negligible (Moucha & Forte, 2011; Walford & White, 2005). In particular, such a rapid uplift is not compatible with geochemical studies of southern Africa Cenozoic uplift, including Partridge (1997), who finds a total uplift of about 600 m during the Neogene, and Flowers and Schoene (2010), who argues for greatly decelerated unroofing in the Cenozoic as compared to during the Mesozoic. Based on studies of the erosion rate during the Cenozoic (Bierman et al., 2014) and sedimentation rates during the Mesozoic (e.g., Ding et al., 2019; Salles et al., 2023), the uplift rate was likely at a maximum during the Mesozoic, followed by a rapid decrease throughout the Cenozoic. The inconsistency between the patterns of dynamic topography (Figure 4g) and vertical displacement (Figure 5) also highlights how the vertical displacement reflects the present-day uplift, not the long-term geologic rate of uplift. While the exact initiation and timing of the uplift of the Southern African Plateau cannot currently be constrained (Artyushkov & Hofmann, 1998; Jones et al., 2017), our results suggest that, at the very least, uplift is ongoing.

5. Conclusions

We computed both global and regional inversions for the radial viscosity profile of the mantle as constrained by the non-hydrostatic geoid. Based on the regional inversions, we can conclude that (a) the viscosity profile beneath southern Africa has a strong lithosphere, a weak asthenosphere and mantle transition zone, a strong mid-mantle punctuated by a low viscosity channel, and a very weak mantle base; and (b) there is internal layering in the African LLSVP, which has a strong upper portion underlain by a much weaker base. By comparing the regional and global inversions, we notice that lateral viscosity variations are an important consideration, as regional differences in viscosity are significant. Our resulting computation of dynamic topography based on the regional inversions allows us to determine that the magnitude of dynamic topography in southern Africa ranges from 1,000

to 2,000 m, with a minimum value near 500 m. The dynamic topography here depends strongly on the choice of scaling profile, highlighting the need for better constraints on the influence of density on seismic velocities in the mantle. Our localization technique for vertical GNSS station motion in southern Africa also indicates that there exists long-wavelength vertical displacement with a mean of 1.5 mm/yr (1σ: 0.8–2.0 mm/yr) within the well-constrained central and southern parts of the region. In summary, a moderate amount of dynamic topography is shown to exist in southern Africa, the formation of which is an ongoing process and spans at least the past several million years.

Data Availability Statement

The code used in this work is available freely online (Harig et al., 2015) as part of the SLEPIAN code package, specifically *Slepian Tango* (https://github.com/csdms-contrib/slepian_tango). Installation instructions for the various Slepian code repositories can be found at http://github.com/Slepian/Slepian. The seismic tomography models used for processing in this study—SEMUCB-WM1 (French & Romanowicz, 2014), SAW642ANb (Panning et al., 2010), S362WMANI+M (Moulik & Ekström, 2014), and S40RTS (Ritsema et al., 2011)—are available at IRIS (Incorporated Research Institutions for Seismology) data center via the IRIS EMC Web Services (https://ds.iris.edu/ds/products/emc/) under open access. The GNSS timeseries (Blewitt et al., 2018) used for processing in this study are available from the University of Nevada Reno Nevada Geodetic Laboratory (http://geodesy.unr.edu/) under open access. Version 1.9 of Hector (Bos et al., 2013) used to compute linear displacement trends for the GNSS timeseries is available via the GNU General License at https://segal.ubi.pt/web-services/whatishector/. The CSR RL05 GRACE timeseries (Save et al., 2016) used for processing in this study are available at http://www2.csr.utexas.edu/grace under open access. The EGM2008 geoid model (Pavlis et al., 2012) used for processing in this study is available via the National Geospatial-Intelligence Agency Office of Geomatics at https://earth-info.nga.mil/ under open access.

Acknowledgments
The authors would like to thank Dr. Nicolas Flament; an anonymous reviewer; and the Editor, Dr. Shin-Chan Han for their constructive comments and suggestions. This work was supported by the National Science Foundation (NSF) via Grant NSF-2142980 funded by the Geophysics program, and by the National Aeronautics and Space Administration (NASA) via Grant NNX17AE18G funded by the Interior of the Earth program, both to C.H. Figures were plotted using the Generic Mapping Tools (Wessel et al., 2013). We would like to thank Dr. Anthony Osei Tutu for his contributions to the development of the software and Dr. Kiriaki Xiluri-Lauria for her tireless technical support.

References

Al-Hajri, Y., White, N. J., & Fishwick, S. (2009). Scales of transient convective support beneath Africa. *Geology*, *37*(10), 883–886. https://doi.org/10.1130/G25703A.1

Amante, C., & Eakins, B. W. (2009). *ETOPO1 1 Arc-minute global relief model: Procedures, data sources and analysis. NOAA technical memorandum NESDIS NGDC-24*. National Geophysical Data Center, NOAA. https://doi.org/10.7289/V5C8276M

Artyushkov, E. V., & Hofmann, A. W. (1998). Neotectonic crustal uplift on the continents and its possible mechanisms. The case of southern Africa. *Surveys in Geophysics*, *19*(5), 369–415. https://doi.org/10.1023/A:1006563824961

Begg, G. C., Griffin, W. L., Natapov, L. M., O'Reilly, S. Y., Grand, S. P., O'Neill, C. J., et al. (2009). The lithospheric architecture of Africa: Seismic tomography, mantle petrology, and tectonic evolution. *Earth and Planetary Science Letters*, *5*(1), 23–50. https://doi.org/10.1130/GES00179.1

Bercovici, D., Ricard, Y., & Richards, M. A. (2000). The relation between mantle dynamics and plate tectonics: A primer. In *The history and dynamics of global plate motions* (pp. 5–46). American Geophysical Union (AGU). https://doi.org/10.1029/GM121p0005

Bierman, P. R., Coppersmith, R., Hanson, K., Neveling, J., Portenga, E. W., & Rood, D. H. (2014). A cosmogenic view of erosion, relief generation, and the age of faulting in southern Africa. *Geological Society of America Today*, *24*(9), 4–11. https://doi.org/10.1130/GSATG206A.1

Blewitt, G., Hammond, W. C., & Kreemer, C. (2018). Harnessing the GPS data explosion for interdisciplinary science [Dataset]. *Eos*, *99*. https://doi.org/10.1029/2018EO104623

Bos, M. S., Fernandes, R. M. S., Williams, S. D. P., & Bastos, L. (2013). Fast error analysis of continuous GNSS observations with missing data [Software]. *Journal of Geodesy*, *87*(4), 351–360. https://doi.org/10.1007/s00190-012-0605-0

Chatelain, J.-L., Molnar, P., Prévot, R., & Isacks, B. (1992). Detachment of part of the downgoing slab and uplift of the New Hebrides (Vanuatu) Islands. *Geophysical Research Letters*, *19*(14), 1507–1510. https://doi.org/10.1029/92GL01389

Colli, L., Ghelichkhan, S., & Bunge, H.-P. (2016). On the ratio of dynamic topography and gravity anomalies in a dynamic Earth. *Geophysical Research Letters*, *43*(6), 2510–2516. https://doi.org/10.1002/2016GL067929

Dahlen, F. A., & Simons, F. J. (2008). Spectral estimation on a sphere in geophysics and cosmology. *Geophysical Journal International*, *174*(3), 774–807. https://doi.org/10.1111/j.1365-246X.2008.03854.x

Davies, D. R., Valentine, A. P., Kramer, S. C., Rawlinson, N., Hoggard, M. J., Eakin, C. M., & Wilson, C. R. (2019). Earth's multi-scale topographic response to global mantle flow. *Nature Geoscience*, *12*(10), 845–850. https://doi.org/10.1038/s41561-019-0441-4

de Wit, M. (2007). The Kalahari epeirogeny and climate change: Differentiating cause and effect from core to space. *South African Journal of Geology*, *110*(2–3), 367–392. https://doi.org/10.2113/gssajg.110.2-3.367

Ding, X., Salles, T., Flament, N., Mallard, C., & Rey, P. F. (2019). Drainage and sedimentary responses to dynamic topography. *Geophysical Research Letters*, *46*(24), 14385–14394. https://doi.org/10.1029/2019GL084400

Emry, E. L., Shen, Y., Nyblade, A. A., Flinders, A., & Bao, X. (2019). Upper mantle Earth structure in Africa from full-wave ambient noise tomography. *Geochemistry, Geophysics, Geosystems*, *20*(1), 120–147. https://doi.org/10.1029/2018GC007804

Farrell, W. E. (1972). Deformation of the earth by surface loads. *Reviews of Geophysics*, *10*(3), 761–797. https://doi.org/10.1029/RG010i003p00761

Fishwick, S. (2010). Surface wave tomography: Imaging of the lithosphere–asthenosphere boundary beneath central and southern Africa? *Lithosphere*, *120*(1–2), 63–73. https://doi.org/10.1016/J.LITHOS.2010.05.011

Flament, N. (2019). Present-day dynamic topography and lower-mantle structure from palaeogeographically constrained mantle flow models. *Geophysical Journal International*, *216*(3), 2158–2182. https://doi.org/10.1093/gji/ggy526

Flament, N., Gurnis, M., & Müller, D. (2013). A review of observations and models of dynamic topography. *Lithosphere*, *5*(2), 189–210. https://doi.org/10.1130/L245.1

Flament, N., Gurnis, M., Williams, S., Seton, M., Skogseid, J., Heine, C., & Dietmar Müller, R. (2014). Topographic asymmetry of the South Atlantic from global models of mantle flow and lithospheric stretching. *Earth and Planetary Science Letters*, *387*, 107–119. https://doi.org/10.1016/J.EPSL.2013.11.017

Flowers, R., & Schoene, B. (2010). U-Th)/He thermochronometry constraints on unroofing of the eastern Kaapvaal craton and significance for uplift of the southern African Plateau. *Geology*, *38*(9), 827–830. https://doi.org/10.1130/G30980.1

Forte, A. M., Peltier, W. R., Dziewonski, A. M., & Woodward, R. L. (1993). Dynamic surface topography: A new interpretation based upon mantle flow models derived from seismic tomography. *Geophysical Research Letters*, *20*(3), 225–228. https://doi.org/10.1029/93GL00249

Forte, A. M., Quéré, S., Moucha, R., Simmons, N. A., Grand, S. P., Mitrovica, J. X., & Rowley, D. B. (2010). Joint seismic–geodynamic-mineral physical modelling of African geodynamics: A reconciliation of deep-mantle convection with surface geophysical constraints. *Earth and Planetary Science Letters*, *295*(3–4), 329–341. https://doi.org/10.1016/J.EPSL.2010.03.017

French, S. W., & Romanowicz, B. A. (2014). Whole-mantle radially anisotropic shear velocity structure from spectral-element waveform tomography [Dataset]. *Geophysical Journal International*, *199*(3), 1303–1327. https://doi.org/10.1093/gji/ggu334

Globig, J., Fernàndez, M., Torne, M., Vergés, J., Robert, A., & Faccenna, C. (2016). New insights into the crust and lithospheric mantle structure of Africa from elevation, geoid, and thermal analysis. *Journal of Geophysical Research: Solid Earth*, *121*(7), 5389–5424. https://doi.org/10.1002/2016JB012972

Green, P. J. (1995). Reversible jump Markov chain Monte Carlo computation and Bayesian model determination. *Biometrika*, *82*(4), 711–732. https://doi.org/10.1093/biomet/82.4.711

Gurnis, M., Mitrovica, J. X., Ritsema, J., & van Heijst, H.-J. (2000). Constraining mantle density structure using geological evidence of surface uplift rates: The case of the African Superplume. *Geochemistry, Geophysics, Geosystems*, *1*(7). https://doi.org/10.1029/1999GC000035

Hager, B. H., & Clayton, R. W. (1989). Constraints on the structure of mantle convection using seismic observations, flow models, and the geoid. In W. R. Peltier (Ed.), *Mantle convection: Plate tectonics and global dynamics* (pp. 657–763).

Hager, B. H., Clayton, R. W., Richards, M. A., Comer, R. P., & Dziewonski, A. M. (1985). Lower mantle heterogeneity, dynamic topography and the geoid. *Nature*, *313*(6003), 541–545. https://doi.org/10.1038/313541a0

Hammond, W. C., Blewitt, G., Kreemer, C., & Nerem, R. S. (2021). GPS imaging of global vertical land motion for studies of sea level rise [Dataset]. *Journal of Geophysical Research: Solid Earth*, *126*(7), e2021JB022355. https://doi.org/10.1029/2021JB022355

Harig, C., Lewis, K. W., Plattner, A., & Simons, F. J. (2015). A suite of software analyzes data on the sphere [Software]. *Eos*, *96*. https://doi.org/10.1029/2015EO025851

Harig, C., & Simons, F. J. (2012). Mapping Greenland's mass loss in space and time. *Proceedings of the National Academy of Sciences* (Vol. 109(49), 19934–19937). https://doi.org/10.1073/pnas.1206785109

Hoggard, M. J., White, N. J., & Al-Attar, D. (2016). Global dynamic topography observations reveal limited influence of large-scale mantle flow. *Nature Geoscience*, *9*(6), 456–463. https://doi.org/10.1038/ngeo2709

Holdt, M. C., White, N. J., Stephenson, S. N., & Conway-Jones, B. W. (2022). Densely sampled global dynamic topographic observations and their significance. *Journal of Geophysical Research: Solid Earth*, *127*(7), e2022JB024391. https://doi.org/10.1029/2022JB024391

Jackson, I., & Faul, U. H. (2010). Grainsize–sensitive viscoelastic relaxation in olivine: Towards a robust laboratory–based model for seismological application. *Physics of the Earth and Planetary Interiors*, *183*(1–2), 151–163. https://doi.org/10.1016/j.pepi.2010.09.005

Jones, A. G., Afonso, J. C., & Fullea, J. (2017). Geochemical and geophysical constrains on the dynamic topography of the Southern African Plateau. *Geochemistry, Geophysics, Geosystems*, *18*(10), 3556–3575. https://doi.org/10.1002/2017GC006908

Knowles, L., Bennett, R. A., & Harig, C. (2020). Vertical displacements of the Amazon basin from GRACE and GPS. *Journal of Geophysical Research: Solid Earth*, *125*(2). https://doi.org/10.1029/2019JB018105

Kolb, J. M., & Lekić, V. (2014). Receiver function deconvolution using transdimensional hierarchical Bayesian inference. *Geophysical Journal International*, *197*(3), 1719–1735. https://doi.org/10.1093/gji/ggu079

Lau, H. C. P., Austermann, J., Mitrovica, J. X., Crawford, O., Al-Attar, D., & Latychev, K. (2018). Inferences of mantle viscosity based on ice age data sets: The bias in radial viscosity profiles due to the neglect of laterally heterogeneous viscosity structure. *Journal of Geophysical Research: Solid Earth*, *123*(9), 7237–7252. https://doi.org/10.1029/2018JB015740

Lau, H. C. P., Mitrovica, J. X., Davis, J. L., Tromp, J., Yang, H. Y., & Al-Attar, D. (2017). Tidal tomography constrains Earth's deep-mantle buoyancy. *Nature*, *551*(7680), 321–326. https://doi.org/10.1038/nature24452

Lee, C.-K., Han, S.-C., & Steinberger, B. (2011). Influence of variable uncertainties in seismic tomography models on constraining mantle viscosity from geoid observations. *Physics of the Earth and Planetary Interiors*, *184*(1), 51–62. https://doi.org/10.1016/j.pepi.2010.10.012

Lekić, V., Cottaar, S., Dziewonski, A., & Romanowicz, B. (2012). Cluster analysis of global lower mantle tomography: A new class of structure and implications for chemical heterogeneity. *Earth and Planetary Science Letters*, *357–358*, 68–77. https://doi.org/10.1016/j.epsl.2012.09.014

Le Stunff, Y., & Ricard, Y. (1997). Partial advection of equidensity surfaces: A solution for the dynamic topography problem? *Journal of Geophysical Research*, *102*(B11), 24655–24667. https://doi.org/10.1029/97JB02346

Lithgow-Bertelloni, C., & Silver, P. G. (1998). Dynamic topography, plate driving forces and the African superswell. *Nature*, *395*(6699), 269–272. https://doi.org/10.1038/26212

Liu, X., & Zhong, S. (2015). The long-wavelength geoid from three-dimensional spherical models of thermal and thermochemical mantle convection. *Journal of Geophysical Research: Solid Earth*, *120*(6), 4572–4596. https://doi.org/10.1002/2015JB012016

Mitrovica, J. X., & Forte, A. M. (2004). A new inference of mantle viscosity based upon joint inversion of convection and glacial isostatic adjustment data. *Earth and Planetary Science Letters*, *225*(1–2), 177–189. https://doi.org/10.1016/J.EPSL.2004.06.005

Molnar, P., England, P. C., & Jones, C. H. (2015). Mantle dynamics, isostasy, and the support of high terrain. *Journal of Geophysical Research: Solid Earth*, *120*(3), 1932–1957. https://doi.org/10.1002/2014JB011724

Morgan, W. J. (1965a). Gravity anomalies and convection currents: 1. A sphere and cylinder sinking beneath the surface of a viscous fluid. *Journal of Geophysical Research*, *70*(24), 6175–6187. https://doi.org/10.1029/JZ070i024p06175

Morgan, W. J. (1965b). Gravity anomalies and convection currents: 2. The Puerto Rico trench and the mid-Atlantic rise. *Journal of Geophysical Research*, *70*(24), 6189–6204. https://doi.org/10.1029/JZ070i024p06189

Moucha, R., & Forte, A. M. (2011). Changes in African topography driven by mantle convection. *Nature Geoscience*, *4*(10), 707–712. https://doi.org/10.1038/ngeo1235

Moucha, R., Forte, A. M., Mitrovica, J. X., & Daradich, A. (2007). Lateral variations in mantle rheology: Implications for convection related surface observables and inferred viscosity models. *Geophysical Journal International*, *169*(1), 113–135. https://doi.org/10.1111/j.1365-246X.2006.03225.x

Moulik, P., & Ekström, G. (2014). An anisotropic shear velocity model of the Earth's mantle using normal modes, body waves, surface waves and long-period waveforms [Dataset]. *Geophysical Journal International*, *199*(3), 1713–1738. https://doi.org/10.1093/gji/ggu356

Panning, M. P., Lekić, V., & Romanowicz, B. A. (2010). Importance of crustal corrections in the development of a new global model of radial anisotropy [Dataset]. *Journal of Geophysical Research*, *115*(B12). B12325. https://doi.org/10.1029/2010JB007520

Partridge, T. (1997). Late Neogene uplift in eastern and southern Africa and its paleoclimatic implications. In *Tectonic uplift and climate change* (pp. 63–86). Springer. https://doi.org/10.1007/978-1-4615-5935-1_4

Pasyanos, M. E., & Nyblade, A. A. (2007). A top to bottom lithospheric study of Africa and Arabia. *Tectonophysics*, *444*(1–4), 27–44. https://doi.org/10.1016/J.TECTO.2007.07.008

Pavlis, N. K., Holmes, S. A., Kenyon, S. C., & Factor, J. K. (2012). The development and evaluation of the earth gravitational model 2008 (EGM2008) [Dataset]. *Journal of Geophysical Research*, *117*(B04406). https://doi.org/10.1029/2011JB008916

Ricard, Y., Fleitout, L., & Froidevaux, C. (1984). Geoid heights and lithospheric stresses for a dynamical earth. *Annales Geophysicae*, *2*, 267–286.

Richards, F. D., Hoggard, M. J., Ghelichkhan, S., Koelemeijer, P., & Lau, H. C. (2023). Geodynamic, geodetic, and seismic constraints favour deflated and dense-cored llvps. *Earth and Planetary Science Letters*, *602*, 117964. https://doi.org/10.1016/j.epsl.2022.117964

Richards, M. A., & Hager, B. H. (1984). Geoid anomalies in a dynamic Earth. *Journal of Geophysical Research*, *89*(B7), 5987–6002. https://doi.org/10.1029/JB089iB07p05987

Ritsema, J., Deuss, A., van Heijst, H.-J., & Woodhouse, J. H. (2011). S40RTS: A degree-40 shear-velocity model for the mantle from new Rayleigh wave dispersion, teleseismic traveltime and normal-mode splitting function measurements [Dataset]. *Geophysical Journal International*, *184*(3), 1223–1236. https://doi.org/10.1111/j.1365-246X.2010.04884.x

Ritsema, J., & Lekić, V. (2020). Heterogeneity of seismic wave velocity in earth's mantle. *Annual Review of Earth and Planetary Sciences*, *48*(1), 377–401. https://doi.org/10.1146/annurev-earth-082119-065909

Rudolph, M. L., Lekić, V., & Lithgow-Bertelloni, C. (2015). Viscosity jump in Earth's mid-mantle. *Science*, *350*(6266), 1349–1352. https://doi.org/10.1126/science.aad1929

Rudolph, M. L., Moulik, P., & Lekić, V. (2020). Bayesian inference of mantle viscosity from whole-mantle density models. *Geochemistry, Geophysics, Geosystems*, *21*(11), e2020GC009335. https://doi.org/10.1029/2020GC009335

Salles, T., Husson, L., Rey, P., Mallard, C., Zahirovic, S., Boggiani, B. H., et al. (2023). Hundred million years of landscape dynamics from catchment to global scale. *Science*, *379*(6635), 918–923. https://doi.org/10.1126/science.add2541

Sambridge, M., Bodin, T., Gallagher, K., & Tkalčić, H. (2013). Transdimensional inference in the geosciences. *Philosophical Transactions of the Royal Society A*, *371*(1984), 20110547. https://doi.org/10.1098/rsta.2011.0547

Saria, E. E., Calais, E., Altamimi, Z., Willis, P., & Farah, H. (2013). A new velocity field for Africa from combined GPS and DORIS space geodetic Solutions: Contribution to the definition of the African reference frame (AFREF). *Journal of Geophysical Research: Solid Earth*, *118*(4), 1677–1697. https://doi.org/10.1002/jgrb.50137

Save, H., Bettadpur, S., & Tapley, B. D. (2016). High-resolution CSR GRACE RL05 mascons [Dataset]. *Journal of Geophysical Research: Solid Earth*, *121*(10), 7547–7569. https://doi.org/10.1002/2016JB013007

Simmons, N. A., Forte, A. M., & Grand, S. P. (2007). Thermochemical structure and dynamics of the African superplume. *Geophysical Research Letters*, *34*(2), L02301. https://doi.org/10.1029/2006GL028009

Simmons, N. A., Forte, A. M., & Grand, S. P. (2009). Joint seismic, geodynamic and mineral physical constraints on three-dimensional mantle heterogeneity: Implications for the relative importance of thermal versus compositional heterogeneity. *Geophysical Journal International*, *177*(3), 1284–1304. https://doi.org/10.1111/j.1365-246X.2009.04133.x

Simons, F. J. (2010). Slepian functions and their use in signal estimation and spectral analysis. In W. Freeden, M. Z. Nashed, & T. Sonar (Eds.), *Handbook of geomathematics* (pp. 891–923). Springer-Verlag. https://doi.org/10.1007/978-3-642-01546-5_30

Simons, F. J., Dahlen, F. A., & Wieczorek, M. A. (2006). Spatiospectral concentration on a sphere. *Society for Industrial and Applied Mathematics*, *48*(3), 504–536. https://doi.org/10.1137/S0036144504445765

Stadler, G., Gurnis, M., Burstedde, C., Wilcox, L. C., Alisic, L., & Ghattas, O. (2010). The dynamics of plate tectonics and mantle flow: From local to global scales. *Science*, *329*(5995), 1033–1038. https://doi.org/10.1126/science.1191223

Steinberger, B. (2016). Topography caused by mantle density variations: Observation-based estimates and models derived from tomography and lithosphere thickness. *Geophysical Journal International*, *205*(1), 604–621. https://doi.org/10.1093/gji/ggw040

Steinberger, B., Conrad, C. P., Osei Tutu, A., & Hoggard, M. J. (2017). On the amplitude of dynamic topography at spherical harmonic degree two. *Tectonophysics*, *760*, 221–228. https://doi.org/10.1016/J.TECTO.2017.11.032

Sun, M., Fu, X., Liu, K. H., & Gao, S. S. (2018). Absence of thermal influence from the African Superswell and cratonic keels on the mantle transition zone beneath southern Africa: Evidence from receiver function imaging. *Earth and Planetary Science Letters*, *503*, 108–117. https://doi.org/10.1016/J.EPSL.2018.09.012

Wahr, J., Molenaar, M., & Bryan, F. (1998). Time variability of the Earth's gravity field: Hydrological and oceanic effects and their possible detection using GRACE. *Journal of Geophysical Research*, *103*(B12), 30205–30229. https://doi.org/10.1029/98JB02844

Walford, H. L., & White, N. J. (2005). Constraining uplift and denudation of west African continental margin by inversion of stacking velocity data. *Journal of Geophysical Research*, *110*(B4). https://doi.org/10.1029/2003JB002893

Wessel, P., Smith, W. H. F., Scharroo, R., Luis, J., & Wobbe, F. (2013). Generic mapping tools: Improved version released. *Eos, Transactions American Geophysical Union*, *94*(45), 409–410. https://doi.org/10.1002/2013EO450001

Wieczorek, M. A., & Simons, F. J. (2005). Localized spectral analysis on the sphere. *Geophysical Journal International*, *162*(3), 655–675. https://doi.org/10.1111/j.1365-246X.2005.02687.x

Yang, T., & Gurnis, M. (2016). Dynamic topography, gravity and the role of lateral viscosity variations from inversion of global mantle flow. *Geophysical Journal International*, *207*(2), 1186–1202. https://doi.org/10.1093/gji/ggw335

Zhang, N., Zhong, S., & Flowers, R. M. (2012). Predicting and testing continental vertical motion histories since the Paleozoic. *Earth and Planetary Science Letters*, *317–318*, 426–435. https://doi.org/10.1016/J.EPSL.2011.10.041